Modular Compact Modeling of MTJ Devices

Mustafa Mert Torunbalci, Pramey Upadhyaya, Sunil A. Bhave, and Kerem Y. Camsari

***Abstract*— This paper describes a robust, modular, and physics-based circuit framework to model the conventional and emerging magnetic tunnel junction (MTJ) devices. Magnetization dynamics are described by the stochastic Landau–Lifshitz–Gilbert (sLLG) equation whose results are rigorously benchmarked with a Fokker–Planck equation description of the magnet dynamics. We then show how sLLG is coupled to the transport equations of MTJ-based devices in a unified circuit platform. Step by step, we illustrate how the physics-based MTJ model can be extended to include different spintronics phenomena, including spin-transfer torque, voltage-controlled magnetic anisotropy (VCMA), and spin–orbit torque phenomena by the experimentally benchmarked examples. To demonstrate how our approach can be used in the exploration of novel MTJ-based devices, we present a recently proposed MEMS resonator-driven spin-torque nano-oscillator (STNO) that can reduce the phase noise of STNOs. We briefly elaborate on the use of our framework beyond conventional devices.**

***Index Terms*— Compact modeling, giant spin Hall effect (GSHE), magnetic tunnel junctions (MTJs), spin-circuits, spin-torque nano-oscillator (STNO), spin-transfer torque (STT)-MRAM, voltage-controlled magnetic anisotropy (VCMA).**

I. Introduction

THE recent progress of spintronics in the past two decades has led to the commercial development of the spin-transfer-torque (STT)-MRAM technology as a low-power and high-speed memory device [1], [2]. Integration of magnetic tunnel junctions (MTJs) with existing CMOS devices has necessitated the development of experimentally informed and physics-based compact models. So far, many MTJ models with varying degrees of sophistication have been developed for circuit simulators, such as SPICE and Verilog-A [3]–[16].

The objective of this paper is to present a compact, physics-based SPICE framework for MTJ-based devices that can incorporate emerging materials and phenomena in a modular fashion. Specifically, our approach has the following distinguishing features.

1) Transport nodes are expressed in terms of "spin-circuits" that generalize the ordinary charge-based networks to include spin and charge currents at each node, generalizing scalar conductances to matrices. This feature enables the modularity of our approach by directly solving for the underlying spin transport equations.
2) Each individual module is carefully benchmarked by a physical theory (e.g., spin-diffusion equations) and/or an experiment with stated assumptions.
3) The framework can easily be extended to build new devices using existing modules; for example, a giant spin Hall effect (GSHE) -driven MTJ is modeled by combining the charge-driven MTJ module with a GSHE module without requiring a new model.

We illustrate the modular circuit framework with different examples. We first validate the nanomagnet dynamics captured by the stochastic Landau–Lifshitz–Gilbert (sLLG) by benchmarking it against a Fokker–Planck equation (FPE) for magnets (see Section II). Next, we briefly describe the individual transport modules (see Section III) and present an experimentally benchmarked STT-MRAM cell (see Section IV). We show how the bias-dependent MTJ model can be extended to capture the voltage-controlled magnetic anisotropy (VCMA) effect. We then switch to three-terminal MTJ devices (see Section VI) and combine the existing MTJ models with benchmarked spin–orbit modules. Finally, we demonstrate how these modules can be combined to describe exploratory and hybrid MTJ devices using the recently proposed MEMS resonator-driven spin-torque nano-oscillators (STNOs) (see Section VII).

In Fig. 1, we show a spin-circuit that is used to model the hybrid MEMS-STNO device discussed in Section VII (see Fig. 6). This example combines most of the modules discussed in this paper and we use it to show explicit circuit schematics of each module. Charge currents and voltages (black lines) are solved according to ordinary circuit theory, whereas spin-currents (blue lines) and magnetization vectors (green lines) are provided to and from the sLLG solver, respectively. It is important to note that the time scales for magnetization dynamics are typically much shorter than typical transport times; therefore, the charge circuit can be treated as a lumped model for each magnetization vector at a given time, allowing well-defined transient simulations. Each example in this paper has been generated from the circuit models shown in Fig. 1 using the parameters defined in Table I.

II. Validation of SPICE-Based SLLG Model

In this section, we show how the SPICE-based sLLG equation is benchmarked by the FPE, closely following the treatment outlined in [19]. Fig. 2 shows how the sLLG equation rigorously reproduces the FPE results. The sLLG equation

Manuscript received April 30, 2018; revised July 6, 2018; accepted July 27, 2018. Date of publication August 21, 2018; date of current version September 20, 2018. This work was supported by the National Science Foundation through the NCN-NEEDS Program, under Contract 1227020-EEC. The review of this paper was arranged by Editor M. M. Cahay. *(Corresponding author: Kerem Y. Camsari.)*

The authors are with the School of Electrical and Computer Engineering, Purdue University, West Lafayette, IN 47907 USA (e-mail: kcamsari@purdue.edu).

Color versions of one or more of the figures in this paper are available online at http://ieeexplore.ieee.org.

Digital Object Identifier 10.1109/TED.2018.2863538

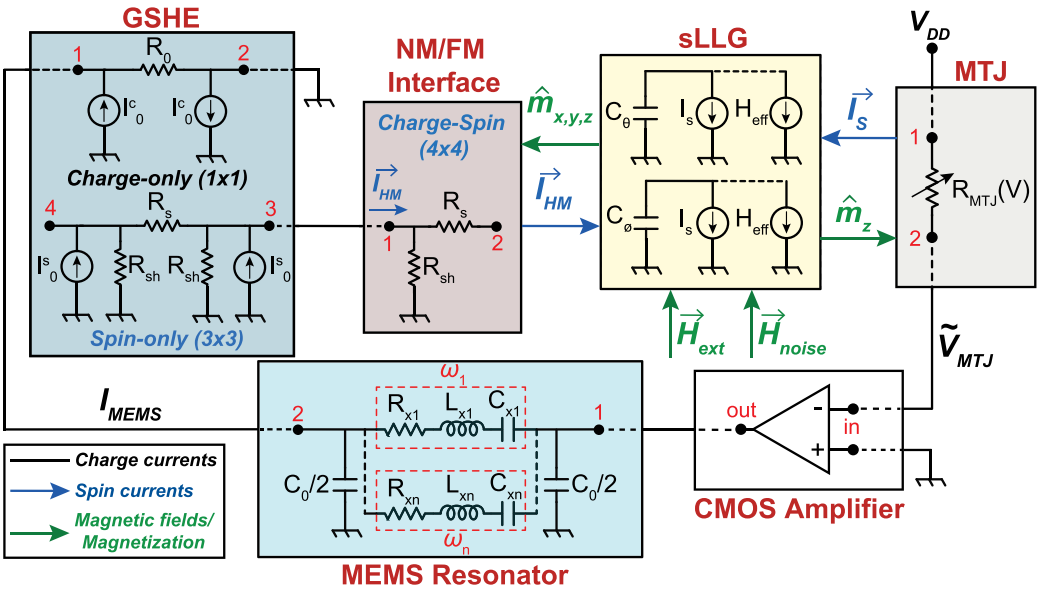

Fig. 1. Modular framework for modeling MTJ-based devices. Explicit circuit schematics for all modules that are used in this paper and used to model the hybrid MEMS-STNO device discussed in Section VII. The circuit connections correspond to the MEMS resonator-driven MTJ-based oscillator that is described in Section VII. This figure also shows how each module interacts with each other. Charge currents and voltages (black lines) are solved according to ordinary circuit theory, whereas spin-currents (blue lines) and magnetization (green lines) are provided to and from the sLLG solver, respectively. sLLG and transport models are described in Sections II and III, respectively. GSHE and NM/FM modules stand for GSHE and NM/FM interface. R_S and R_{sh} stand for series and shunt resistances. BVD equivalent circuit is used to model MEMS resonators [17]. PTMs are used for CMOS circuits [18].

is solved by the transient noise feature (.trannoise) of the HSPICE simulator; however, the equations and circuits are simulator independent and can be implemented by powerful circuit platforms, such as MAPP [20]. Our implementation uses spherical coordinates to solve the LLG equation, but the noise field is input in the Cartesian coordinates and added to any other external magnetic field before being expressed in spherical coordinates for the LLG solver. The LLG equation in the monodomain approximation reads

$$(1+\alpha^2)\frac{d\hat{m}_i}{dt} = -|\gamma|d\hat{m}_i \times \vec{H}_{\text{eff}} - \alpha|\gamma|(\hat{m}_i \times \hat{m}_i \times \vec{H}_{\text{eff}}) + \frac{1}{qN_s}(\hat{m}_i \times \vec{I}_s \times \hat{m}_i) + \frac{\alpha}{qN_s}(\hat{m}_i \times \vec{I}_s) \quad (1)$$

where $\hat{m}_i$ is the unit vector along the magnetization, γ is the gyromagnetic ratio, α is the damping constant, and $\vec{I}_s$ is the total spin-current. N_s is the total number of spins given by $N_s = M_s \text{V}_{\text{free}}/\mu_{\text{B}}$, where M_s is the saturation magnetization, V_{free} is the volume of the free layer (FL), μ_B is the Bohr magneton, and $\vec{H}_{\text{eff}}$ is the effective magnetic field, including the uniaxial, shape anisotropy, and magnetic thermal noise terms. The magnetic thermal noise ($\vec{H}_n$) enters as an additional magnetic field in 3-D with the following mean and variance, uncorrelated in all three directions:

$$\langle H_n^{x,y,z}\rangle = 0 \quad \text{and} \quad \langle (H_n^{x,y,z})^2\rangle = \frac{2\alpha kT}{\gamma M_s V} \quad (2)$$

where k is the Boltzmann's constant and T is the temperature. The model becomes more accurate as devices are scaled down, maintaining the single-domain approximation.

As shown in [19], FPE reduces to a simple boundary value problem for magnets with perpendicular anisotropy, as long as all the external fields and currents are confined to the direction of the easy axis ($\pm z$-direction). FPE describes the dynamics of a *probability density*, while the sLLG tracks the dynamics of a single nanomagnet and requires ensemble averaging to be compared with FPE. 1-D FPE reads

$$\frac{\partial \rho(m_z,\tau)}{\partial \tau} = \frac{\partial}{\partial m_z}\left[(i-h-m_z)(1-m_z^2)\rho + \frac{1-m_z^2}{2\Delta}\frac{\partial \rho}{\partial m_z}\right] \quad (3)$$

where τ is a normalized time in terms of the damping coefficient α, the uniaxial anisotropy constant H_k, and the gyromagnetic ratio γ, such that $t = \tau(1+\alpha^2)/(\alpha\gamma H_k)$, and t denotes real time. Δ represents the normalized energy barrier of the magnet $(\Delta)kT$ representing the total energy barrier. The input spin-current, i, and the external magnetic field, h, are both in the $\pm z$-direction, and they are normalized by I_{sc} and H_k, respectively, where I_{sc} is given by $4\,q/\hbar\alpha\Delta(kT)$. When the results of FPE and sLLG are compared for a spin-current input i, the corresponding current $i \times I_{\text{sc}}$ must be used for sLLG.

Since (3) is a 1-D boundary value problem, we can solve it using the bvp4c function of MATLAB, subject to the boundary condition $\partial\rho(m_z,\tau)/\partial m_z = 0$ at $m_z = \pm 1$ and to the initial condition

$$\rho(m_z, \tau = 0) = \frac{1}{Z}\exp\left[-\Delta\left(1-m_z^2\right)\right]\Theta(m_z) \quad (4)$$

where Z is a normalization constant ensuring $\int dm_z\,\rho(m_z) = 1$ in the range $(-1,+1)$ and $\Theta(m_z)$ is the Heaviside function so that the symmetric magnetization probability is broken to start from a given distribution, in this case chosen to be close

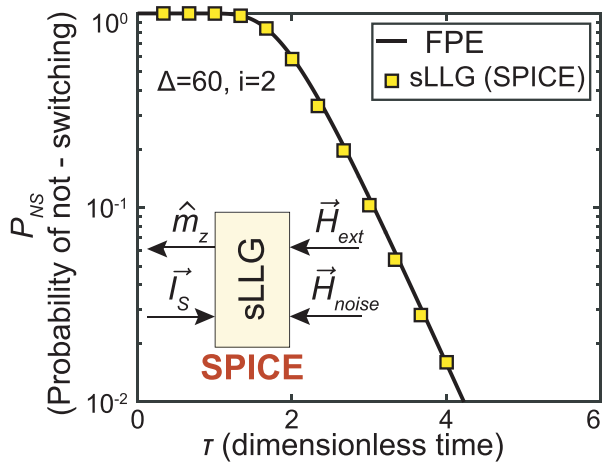

Fig. 2. FPE versus sLLG comparison. An ensemble of magnets ($N = 1000$) with perpendicular anisotropy with a 60-kT energy barrier is subject to a spin-current in the $-z$-direction twice the critical spin-current. Probability of not switching ($P_{\rm NS}$) is obtained from a numerical solution of FPE (black solid lines) and compared with the SPICE-based sLLG as explained in this paper.

to $m_z = 1$. Note that the full FPE equation requires a more general PDE solver (2-D), for example, in the case of an in-plane magnet that contains fields in directions other than the easy axis [21].

The procedure of comparing FPE with sLLG is as follows.

1) Prepare 1000 identical samples that start at $m_z = +1$ at $t = 0$ for the sLLG simulation.
2) Wait for 5 ns for identical samples to thermalize and approximately form a Boltzmann distributed initial ensemble.
3) Apply spin-current in the $-z$-direction ($I_s = i \times I_{sc}$, $i = 2$) at 5 ns.
4) Measure the *last* m_z value at each time point for each ensemble.
5) Obtain $P_{\rm NS}(\tau)$ by counting the number of samples with m_z values that are greater than 0 (not switched) and normalizing to sample size, $N = 1000$ (each yellow square in Fig. 2).
6) Solve FPE numerically as a function of τ to obtain $\rho(m_z, \tau)$.
7) Obtain $P_{\rm NS}(\tau)$ from the integral

$$\int_{m_z=0}^{m_z=+1} dm_z \rho(m_z, \tau). \tag{5}$$

8) Compare $P_{\rm NS}$-FPE with $P_{\rm NS}$-LLG (see Fig. 2).

Note how in the second step, the requirement of a Boltzmann distributed initial ensemble is obtained naturally by running the sLLG equation for a few nanoseconds so that each sample receives a random initial angle sampled from the correct equilibrium distribution in accordance with the initial condition used for the FPE.

This precise an agreement between the FPE method and the sLLG (Fig. 2) despite the elaborate comparison of the two completely different methods establishes the validity of our HSPICE-based sLLG model. This result is consistent with careful studies that have investigated the numerical solution of the sLLG equation [22]–[24].

III. Description of Transport Models

In this section, we describe the transport models that are solved self-consistently with the sLLG model that takes spin-currents, either due to STTs or spin–orbit torques (SOTs), as an input.

A. Giant Spin Hall Effect

To model the GSHE-induced spin–orbit currents, we use a spin-circuit description whose results are shown to be equivalent to the spin-diffusion equations [25]. Under short-circuit (spin–sink) conditions, this model produces a spin-current that is proportional to a charge current I_c

$$\beta = \frac{I_{\rm HM}}{I_c} = \theta \frac{l_{\rm HM}}{t_{\rm HM}} \left(1 - \sec\left[\frac{t_{\rm HM}}{\lambda_{\rm sf}}\right]\right) \tag{6}$$

where θ is the spin Hall angle, $l_{\rm HM}$ and $t_{\rm HM}$ are the length and thickness, and $\lambda_{\rm sf}$ is the spin–flip length of the heavy metal (HM). The GSHE module is implemented as two coupled circuits: one describing the charge transport (in the longitudinal direction) and the other describing the spin transport (in the transverse direction) in terms of 3-D spin-currents and voltages [25].

B. Normal Metal/Ferromagnet Interface

This module represents the interface between a normal metal (FM) and a ferromagnet (FM) in terms of the microscopic "mixing conductances" that describe the transmission and reflection of spin-currents incident to an FM from a metal [26], [27]. For sufficiently large mixing conductances, the incident spin-current is transferred to the FM with 100% efficiency (spin–sink). Combined with the GSHE module, the interface circuit can reduce the spin-current efficiency to less than 100% and capture subtle physical effects, such as spin Hall magnetoresistance [25]. The details of the interface between a HM and the FM are believed to play an important role as recent studies suggest [28], and the NM/FM interface circuit can be modified to include these phenomena in the future.

C. MTJ

The bias dependence of the MTJ is captured by assuming voltage-dependent interface polarizations $P(V)$. This observation is supported by a microscopic nonequilibrium Green's function-based quantum transport model [29], [30]. This physically motivated assumption may not precisely fit the bias dependence of MTJs for any given device; however, we believe that it can be useful in modeling more complicated junctions involving multiple interfaces [31].

In this picture, the MTJ conductance is expressed as

$$G_{\rm MTJ}(V) = G_0[1 + P_1(V)P_2(-V)\cos(\theta)] \tag{7}$$

where G_0 is the average MTJ conductance $(G_P + G_{\rm AP})/2$, V is the voltage drop across the junction, and $P_1(V) = P_2(-V)$

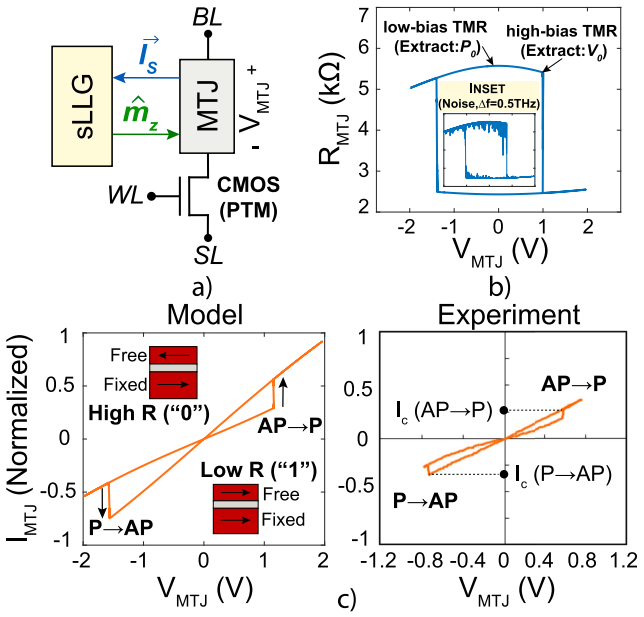

Fig. 3. STT-MRAM [33]. (a) Spin-circuit modeling of an STT-MRAM cell, consisting of a two-terminal MTJ in series with an access transistor. (b) Bias-dependent TMR is used to extract the parameters P_0 and V_0 of (8). Inset: stochastic simulation for one sample. (c) Experimental benchmarking of the STT-MRAM. In the simulation, MTJ voltage is swept from negative to positive, while I–V characteristics are being monitored. Therefore, the circuit produces the I–V characteristics in one long transient simulation solving sLLG and transport equations self-consistently. Experimental figure is reprinted with permission from [33].

are the voltage-dependent interface polarizations for the free and fixed layers, respectively, assuming a symmetric junction. θ describes the angle between the fixed layer and the FL. We postulate the voltage-dependent polarizations as

$$P_{1,2}(V) = \frac{1}{1 + P_0 \exp(-V/V_0)} \tag{8}$$

where the parameter P_0 is determined by the low-bias tunneling magnetoresistance (TMR) and V_0 is determined by the high-bias features of TMR (see Fig. 3). V_0 is assumed to be the same for fixed and FL interfaces assuming symmetric junctions throughout this paper. This functional form of the bias-dependent interface polarization could explain the observed switching asymmetry between V(P→AP) and V(AP→P) [29] and the bias dependence of in-plane and out-of-plane torques. In our model, the spin-current (in-plane) incident to the FL is given by $\vec{I}_S = P_2(V)(G_0)\hat{M}$, where P_2 is the interface polarization of the fixed layer, G_0 is the average MTJ conductance, and $\hat{M}$ is the magnetization direction of the fixed layer, as discussed in [29]. Physically, the spin-current incident to the FL is proportional to the polarization of the fixed layer, capturing the angular dependence of the in-plane spin-currents [32]. The out-of-plane spin-current can similarly be included, but we assume it to be zero in the examples shown in this paper.

IV. STT-MRAM

A simple STT-MRAM cell consists of a two-terminal MTJ in series with an access transistor (1T/1MTJ), where the data are stored in the FL magnetization. Unlike traditional MRAM that uses magnetic fields, the FL magnetization is switched by passing a charge current through the fixed layer that gets spin polarized for writing information. This can be done by applying proper voltages to the bitline and the source line while keeping the access transistor ON with the appropriate word-line voltage (see Fig. 3).

In this section, we present an experimental benchmarking of an STT-MRAM cell [33] that consists of two-terminal MTJ with an access transistor embedded into a 45-nm CMOS technology. We use 14-nm high performance-FinFET models using the predictive technology models (PTMs) [18] with no significant difference in the final results.

For all MTJs described in this paper, our methodology to reproduce the MTJ characteristics is as follows.

1) Use low-bias TMR to obtain the parameter P_0 from Julliere's formula TMR $= 2P^2(V=0)/[1-P^2(V=0)]$.
2) Use high-bias TMR to obtain the parameter V_0.
3) Predict switching characteristics *only using* P_0, V_0, and magnet parameters with no additional fitting parameters.

Fig. 3(a) and (b) presents the spin-circuit model and experimental benchmarking of the STT-MRAM cell in [33]. Due to missing material information in this experiment, we assume CoFeB parameters for free and fixed layers and use typical values for M_s, H_d, and α, as shown in Table I, obtaining reasonable agreement with the experiment. Our model captures the bias dependence of TMR as well as the in-plane torque asymmetry by using the voltage-dependent interface polarizations $P_1(V)$ and $P_2(-V)$ resulting in a higher write current for P-to-AP switching compared to AP-to-P switching [29].

TABLE I
PARAMETERS USED FOR ALL SIMULATIONS

STT-MRAM [33]	
V_{free}	100 nm × 40 nm × 1.5 nm
M_s, α, H_k, H_d	1100 emu/cc, 0.01, 150 Oe, 1.3 T
TMR, P_0, V_0	110%, 0.6887, 1.81
CMOS models, Size	14 nm HP-FinFET, nfin=50
t_{sim}, t_{step} (HSPICE, noise:on)	5 μs, 2 ps
VCMA [34]	
V_{free}	70 nm × 70 nm × 1.8 nm
M_s, α, $H_k = H_{ks} - H_d$	1100 emu/cc, 0.075, 120 Oe
TMR, P_0, V_0	150%, 0.5253, 0.33
t_{ox}, η	1.4 nm, 6.5 $\mu J/m^2$/V/nm
t_{sim}, t_{step} (HSPICE, noise:off)	25 μs, 5 ps
GSHE-driven MTJ [36]	
V_{free}	350 nm × 100 nm × 1.6 nm
M_s, α, H_k, H_d	1100 emu/cc, 0.021, 40 Oe, 0.76 T
TMR, P_0, V_0, Re[G_{mix}]	50%, 1.13, 0.083, 10^{15} S/m^2
θ_{HM}, λ_{HM}, ρ_{HM} (HM=Ta)	0.12, 1.5 nm, 190 $\mu\Omega - cm$
l_{HM}, w_{HM}, t_{HM}	1 μm, 5 μm, 6.2 nm
t_{sim}, t_{step}, (HSPICE, noise:on)	10 μs, 2 ps

V. VOLTAGE-CONTROLLED MAGNETIC ANISOTROPY

In recent years, enormous progress has been made in the voltage control of magnetism. A notable example is the VCMA effect, where the electric field across a two-terminal MTJ, in particular with PMA magnets, induces a change in the magnetic anisotropy (see [34], [35]). Fig. 4(a) and (b) shows

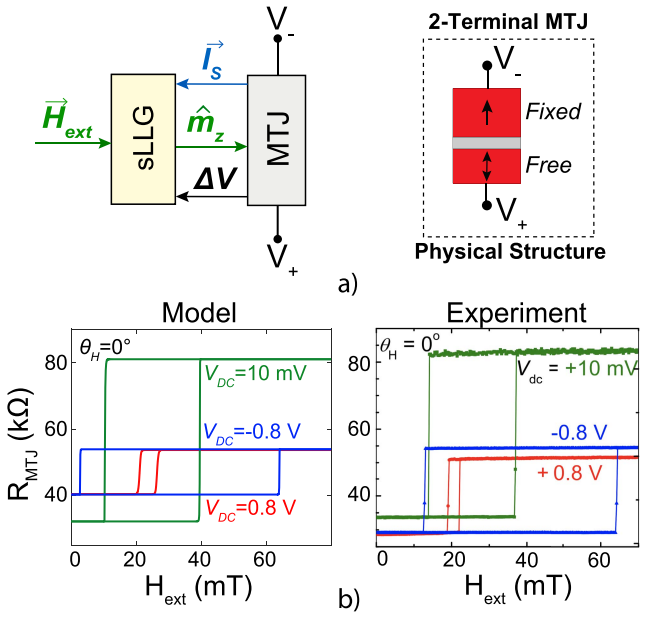

Fig. 4. VCMA [34]. (a) Spin-circuit model for the VCMA effect. LLG solver receives the voltage across the MTJ as an additional input to modulate the magnetic anisotropy. This change in anisotropy is modeled as a magnetic field that is dependent on instantaneous magnetization $\Delta H_k m_z$. (b) Experimental benchmarking of the VCMA effect at different voltages. A 25-mT constant dipolar shift is added. The shifts in the central dipolar fields at different voltages are due to the spin-current flowing in the MTJ. Experimental figure is reprinted with permission from [34].

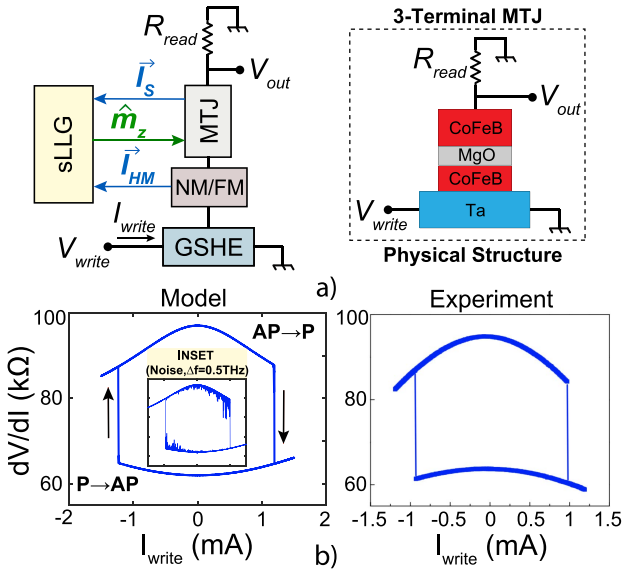

Fig. 5. GSHE-driven MTJ [36]. (a) Spin-circuit model and physical implementation of a GSHE-driven MTJ. (b) Experimental benchmarking of the GSHE-driven MTJ. In the simulation, current through the HM is slowly swept from negative to positive, while MTJ resistance is being monitored, as in previous examples. Parameters P_0 and V_0 are obtained from bias dependence of TMR. Inset: stochastic simulation for one sample. Experimental figure is reprinted with permission from [36].

how the bias-dependent MTJ model discussed in Section IV can be extended to include the VCMA effect.

The coercivity of the PMA FL under low-bias conditions is likely to depend on the applied pulsewidth and thermal activation. For simplicity, we assume this coercivity is equal to the uniaxial anisotropy (H_k) in a monodomain approximation while noting that this assumption could underestimate the extracted VCMA coefficient. We assume a linear modification of the FL anisotropy with respect to voltage

$$H_k(V) = H_{k0} + \frac{V}{t_{\text{ox}}}\left(\frac{\eta}{t_{\text{fm}} M_s}\right) \tag{9}$$

where t_{fm} and t_{ox} are the oxide and FL thickness, η is the VCMA coefficient (in μJ /m^2/V/nm), and V is the applied voltage. Combined with the bias-dependent MTJ, our VCMA model seems to capture three distinct effects, as shown in Fig. 4: 1) the H_k modulation of the FL; 2) the bias dependence of the MTJ, where $\pm$0.8 V decreases the TMR; and 3) the shift of the hysteresis loop that arises due to a spin-current flowing from the fixed layer to the FL in opposite directions for opposite voltage polarity. The asymmetric shift for $\pm$0.8 V seems consistent with the asymmetry in the magnitude of the spin-current captured by the voltage-dependent polarizations. Note that only the first effect is added explicitly, the rest follows from the MTJ model discussed in Section IV.

VI. GSHE-Driven MTJ

An SOT-MRAM cell consists of a three-terminal MTJ and access transistors, where spin-current is generated by passing a charge current through a HM for writing information. Thus, SOT-MRAM achieves read and write operations using separate paths, improving a feature of STT-MRAMs that use same paths for read and write. In this section, we experimentally benchmark a GSHE-driven MTJ (without the transistor periphery) that consists of an in-plane CoFeB for fixed and FLs and Tantalum for the HM. Fig. 5(a) shows spin-circuit modeling and physical implementation of the GSHE-driven MTJ in [36]. We follow the same methodology to reproduce the MTJ characteristics explained in Section IV using identical material and device parameters as in the experiment. Fig. 5(b) compares our results with the experiment that seem to be in good quantitative agreement without any additional fitting parameters. We note, however, the switching currents in the experiment could also be influenced by thermal activation mechanisms and multidomain features that are not included in our model. The symmetric switching currents as well as the roll-off due to high-bias MTJ properties are captured although the pronounced (and opposite) roll-off in the parallel TMR branch suggests mechanisms beyond what is in our model, possibly related to multidomain features of the nanomagnets.

VII. MEMS Resonator-Driven STNO

In this section, our purpose is to show how the circuit framework that we present can be used to evaluate exploratory devices using a recently proposed hybrid MTJ-based device as an example. It is well-established that the FL of an MTJ can be driven to function as a nano-oscillator by STT and SOT mechanisms [37]. However, these STNOs suffer from very poor phase-noise characteristics [38], limiting their potential as nanoscale, tunable oscillators.

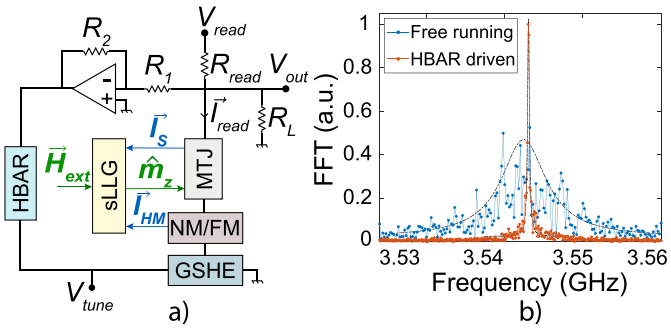

Fig. 6. HBAR-driven STNO with current feedback. (a) Spin-circuit modeling of an MEMS resonator-driven STNO. The frequency spectrum is obtained by taking the FFT of the time-domain signal. (b) FFT spectra of free-running STNO and HBAR-driven STNO. A Lorentzian function is used to fit the FFT data to extract the linewidth of the oscillators. HBAR-driven STNO shows ∼15× enhancement in the quality factor.

A recent proposal suggested the coupling of GSHE-driven STNOs with very high-quality MEMS-resonators as a CMOS-compatible solution to improve the phase-noise characteristics of STNOs [39]. This concept is tested by combining a high-overtone bulk acoustic wave resonator (HBAR) and three-terminal MTJ-based STNO. The 2-port HBAR is described by the Butterworth–Van Dyke (BVD) equivalent circuit [17], coupled to the GSHE-driven MTJ with current feedback. The full spin-circuit corresponding to this example is shown in Fig. 1. We use similar parameters for the GSHE-driven MTJ that is described in Section VI. Fig. 6 presents the hybrid model and compares FFT spectra of a free-running STNO and an HBAR-driven STNO, where HBAR-driven STNO exhibits a significant enhancement in the oscillator linewidth. Furthermore, the original tunability of the STNO is maintained by locking it to the nearest high Q peak of the HBAR. This example demonstrates how our modular framework can be combined with established circuit models to propose and evaluate hybrid devices involving MTJs.

VIII. Beyond Conventional Devices

The modular framework we present in this paper can be used beyond compact modeling MTJ devices that are envisioned in the context of memory applications [2]. For example, materials, such as topological insulators, exhibiting spin–momentum locking (SML) have been expressed in terms of general spin-circuit models recently [40], [41]. In conjunction with the nanomagnet modules discussed in this paper, such SML models have been used in an exploratory mode to propose new memory devices [42] and to model novel devices exhibiting three resistance states [40] that have subsequently received experimental confirmation [43]. In addition, the benchmarked stochastic LLG solver coupled with MTJ modules has been used to model a special type of superparamagnetic MTJs [44] functioning as three-terminal tunable random number generators [45], or probabilistic bits (p-bits), and p-circuits built out of such p-bits have been shown to be useful for a wide range of applications, such as Ising computing [46], Bayesian inference [47], and invertible logic [48].

IX. Conclusion

We present a modular, extensible, and physics-based circuit framework for MTJ devices that can capture a wide range of spintronic phenomena. We start by a rigorous validation of the stochastic LLG model and then demonstrate our approach with a step-by-step extension of our framework. The same basic models are used to capture bias dependence of MTJs to model STT-MRAM, GSHE-driven MTJs, VCMA-based MTJs, as well as hybrid circuits, such as MEMS resonator-driven STNOs. We believe that the modular framework presented here can be an important compact modeling toolbox in the exploration of new MTJ devices as the fields of spintronics and magnetism progress with new materials and phenomena.

References

[1] W. J. Gallagher and S. S. P. Parkin, "Development of the magnetic tunnel junction MRAM at IBM: From first junctions to a 16-Mb MRAM demonstrator chip," *IBM J. Res. Develop.*, vol. 50, no. 1, pp. 5–23, Jan. 2006, doi: 10.1147/rd.501.0005.

[2] S. Bhatti, R. Sbiaa, A. Hirohata, H. Ohno, S. Fukami, and S. Piramanayagam, "Spintronics based random access memory: A review," *Mater. Today*, vol. 20, no. 9, pp. 530–548, 2017, doi: 10.1016/j.mattod.2017.07.007.

[3] L.-B. Faber, W. Zhao, J.-O. Klein, T. Devolder, and C. Chappert, "Dynamic compact model of spin-transfer torque based magnetic tunnel junction (MTJ)," in *Proc. IEEE 4th Int. Conf. Design Technol. Integr. Syst. Nanoscal Era (DTIS)*, Apr. 2009, pp. 130–135, doi: 10.1109/DTIS.2009.4938040.

[4] W. Guo *et al.*, "SPICE modelling of magnetic tunnel junctions written by spin-transfer torque," *J. Phys. D, Appl. Phys.*, vol. 43, no. 21, p. 215001, 2010, doi: 10.1088/0022-3727/43/21/215001.

[5] K. Munira, W. H. Butler, and A. W. Ghosh, "A quasi-analytical model for energy-delay-reliability tradeoff studies during write operations in a perpendicular STT-RAM cell," *IEEE Trans. Electron Devices*, vol. 59, no. 8, pp. 2221–2226, Aug. 2012, doi: 10.1109/TED.2012.2198825.

[6] G. D. Panagopoulos, C. Augustine, and K. Roy, "Physics-based SPICE-compatible compact model for simulating hybrid MTJ/CMOS circuits," *IEEE Trans. Electron Devices*, vol. 60, no. 9, pp. 2808–2814, Sep. 2013, doi: 10.1109/TED.2013.2275082.

[7] S. Manipatruni, D. E. Nikonov, and I. A. Young, "Vector spin modeling for magnetic tunnel junctions with voltage dependent effects," *J. Appl. Phys.*, vol. 115, no. 17, p. 17B754, 2014, doi: 10.1063/1.4868495.

[8] K. Jabeur, F. Bernard-Granger, G. Di Pendina, G. Prenat, and B. Dieny, "Comparison of verilog—A compact modelling strategies for spintronic devices," *Electron. Lett.*, vol. 50, no. 19, pp. 1353–1355, 2014, doi: 10.1049/el.2014.1083.

[9] Y. Zhang *et al.*, "Compact model of subvolume MTJ and its design application at nanoscale technology nodes," *IEEE Trans. Electron Devices*, vol. 62, no. 6, pp. 2048–2055, Jun. 2015, doi: 10.1109/TED.2015.2414721.

[10] T. Chen *et al.*, "Comprehensive and macrospin-based magnetic tunnel junction spin torque oscillator model-part I: Analytical model of the MTJ STO," *IEEE Trans. Electron Devices*, vol. 62, no. 3, pp. 1037–1044, Mar. 2015, doi: 10.1109/TED.2015.2390676.

[11] J. Kim, A. Chen, B. Behin-Aein, S. Kumar, J.-P. Wang, and C. H. Kim, "A technology-agnostic MTJ spice model with user-defined dimensions for STT-MRAM scalability studies," in *Proc. IEEE Custom Integr. Circuits Conf. (CICC)*, Sep. 2015, pp. 1–4, doi: 10.1109/CICC.2015.7338407.

[12] K. Y. Camsari, S. Ganguly, and S. Datta, "Modular approach to spintronics," *Sci. Rep.*, vol. 5, Jun. 2015, Art. no. 10571, doi: 10.1038/srep10571.

[13] M. Kazemi, G. E. Rowlands, E. Ipek, R. A. Buhrman, and E. G. Friedman, "Compact model for spin–orbit magnetic tunnel junctions," *IEEE Trans. Electron Devices*, vol. 63, no. 2, pp. 848–855, Feb. 2016, doi: 10.1109/TED.2015.2510543.

[14] K. Y. Camsari, S. Ganguly, and D. Datta, "A modular spin-circuit model for magnetic tunnel junction devices," in *Proc. IEEE 74th Annu. Device Res. Conf. (DRC)*, Jun. 2016, pp. 1–2, doi: 10.1109/DRC.2016.7673632.

[15] R. De Rose *et al.*, "A compact model with spin-polarization asymmetry for nanoscaled perpendicular MTJs," *IEEE Trans. Electron Devices*, vol. 64, no. 10, pp. 4346–4353, Oct. 2017, doi: 10.1109/TED.2017.2734967.

[16] *Modular Approach to Spintronics*. Accessed: Apr. 2018. [Online]. Available: https://nanohub.org/groups/spintronics

[17] J. D. Larson, III, P. D. Bradley, S. Wartenberg, and R. C. Ruby, "Modified Butterworth-van Dyke circuit for FBAR resonators and automated measurement system," in *Proc. IEEE Ultrason. Symp.*, vol. 1, Oct. 2000, pp. 863–868, doi: 10.1109/ULTSYM.2000.922679.

[18] Y. Cao, T. Sato, D. Sylvester, M. Orshansky, and C. Hu. (2002). *Predictive Technology Model*. [Online]. Available: https://www.ptm.asu.edu

[19] W. H. Butler *et al.*, "Switching distributions for perpendicular spin-torque devices within the macrospin approximation," *IEEE Trans. Magn.*, vol. 48, no. 12, pp. 4684–4700, Dec. 2012, doi: 10.1109/TMAG.2012.2209122.

[20] T. Wang and J. Roychowdhury, "Multiphysics modelling and simulation in Berkeley MAPP," in *Proc. IEEE MTT-S Int. Conf. Numer. Electromagn. Multiphys. Modeling Optim. (NEMO)*, Jul. 2016, pp. 1–3, doi: 10.1109/NEMO.2016.7561645.

[21] Y. Xie, B. Behin-Aein, and A. W. Ghosh, "Fokker—Planck study of parameter dependence on write error slope in spin-torque switching," *IEEE Trans. Electron Devices*, vol. 64, no. 1, pp. 319–324, Jan. 2017, doi: 10.1109/TED.2016.2632438.

[22] J. L. García-Palacios and F. J. Lázaro, "Langevin-dynamics study of the dynamical properties of small magnetic particles," *Phys. Rev. B, Condens. Matter*, vol. 58, no. 22, p. 14937, 1998, doi: 10.1103/PhysRevB.58.14937.

[23] A. S. Roy, A. Sarkar, and S. P. Mudanai, "Compact modeling of magnetic tunneling junctions," *IEEE Trans. Electron Devices*, vol. 63, no. 2, pp. 652–658, Feb. 2016, doi: 10.1109/NEWCAS.2008.4606363.

[24] S. Ament, N. Rangarajan, A. Parthasarathy, and S. Rakheja. (Jul. 2016). "Solving the stochastic Landau-Lifshitz-Gilbert-Slonczewski equation for monodomain nanomagnets: A survey and analysis of numerical techniques." [Online]. Available: https://arxiv.org/abs/1607.04596

[25] S. Hong, S. Sayed, and S. Datta, "Spin circuit representation for the spin Hall effect," *IEEE Trans. Nanotechnol.*, vol. 15, no. 2, pp. 225–236, Mar. 2016, doi: 10.1109/TNANO.2016.2514410.

[26] A. Brataas, G. E. W. Bauer, and P. J. Kelly, "Non-collinear magnetoelectronics," *Phys. Rep.*, vol. 427, no. 4, pp. 157–255, 2006, doi: 10.1016/j.physrep.2006.01.001.

[27] S. Srinivasan, V. Diep, B. Behin-Aein, A. Sarkar, and S. Datta, "Modeling multi-magnet networks interacting via spin currents," in *Handbook of Spintronics*. Springer, 2014, pp. 1–49, doi: 10.1007/978-94-007-6892-5_46.

[28] S. Shi, Y. Ou, S. Aradhya, D. C. Ralph, and R. A. Buhrman, "Fast low-current spin-orbit-torque switching of magnetic tunnel junctions through atomic modifications of the free-layer interfaces," *Phys. Rev. Appl.*, vol. 9, no. 1, p. 011002, 2018, doi: 10.1103/PhysRevApplied.9.011002.

[29] D. Datta, B. Behin-Aein, S. Datta, and S. Salahuddin, "Voltage asymmetry of spin-transfer torques," *IEEE Trans. Nanotechnol.*, vol. 11, no. 2, pp. 261–272, Mar. 2012, doi: 10.1109/TNANO.2011.2163147.

[30] D. Datta *et al.*, "Quantitative model for switching asymmetry in perpendicular MTJ: A material-device-circuit co-design," in *IEDM Tech. Dig.*, Dec. 2017, pp. 5–31, doi: 10.1109/IEDM.2017.8268482.

[31] H. Sato *et al.*, "Comprehensive study of CoFeB-MgO magnetic tunnel junction characteristics with single- and double-interface scaling down to 1X nm," in *IEDM Tech. Dig.*, Dec. 2013, pp. 3.2.1–3.2.4, doi: 10.1109/IEDM.2013.6724550.

[32] K. Y. Camsari, S. Ganguly, D. Datta, and S. Datta, "Physics-based factorization of magnetic tunnel junctions for modeling and circuit simulation," in *IEDM Tech. Dig.*, Dec. 2014, pp. 6–35, doi: 10.1109/IEDM.2014.7047177.

[33] C. J. Lin *et al.*, "45 nm low power CMOS logic compatible embedded STT MRAM utilizing a reverse-connection 1T/1MTJ cell," in *IEDM Tech. Dig.*, Dec. 2009, pp. 1–4, doi: 10.1109/IEDM.2009.5424368.

[34] S. Kanai, M. Yamanouchi, S. Ikeda, Y. Nakatani, F. Matsukura, and H. Ohno, "Electric field-induced magnetization reversal in a perpendicular-anisotropy CoFeB-MgO magnetic tunnel junction," *Appl. Phys. Lett.*, vol. 101, no. 12, p. 122403, 2012, doi: 10.1063/1.4753816.

[35] P. K. Amiri and K. L. Wang, "Voltage-controlled magnetic anisotropy in spintronic devices," *Spin*, vol. 2, no. 3, p. 1240002, 2012, doi: 10.1142/S2010324712400024.

[36] L. Liu, C.-F. Pai, Y. Li, H. W. Tseng, D. C. Ralph, and R. A. Buhrman, "Spin-torque switching with the giant spin Hall effect of tantalum," *Science*, vol. 336, no. 6081, pp. 555–558, May 2012, doi: 10.1126/science.1218197.

[37] T. Chen *et al.*, "Spin-torque and spin-Hall nano-oscillators," *Proc. IEEE*, vol. 104, no. 10, pp. 1919–1945, Oct. 2016, doi: 10.1109/JPROC.2016.2554518.

[38] M. Quinsat *et al.*, "Amplitude and phase noise of magnetic tunnel junction oscillators," *Appl. Phys. Lett.*, vol. 97, no. 18, p. 182507, 2010, doi: 10.1063/1.3506901.

[39] M. M. Torunbalci, T. A. Gosavi, K. Y. Camsari, and S. A. Bhave, "Magneto acoustic spin Hall oscillators," *Sci. Rep.*, vol. 8, no. 1, 2018, Art. no. 1119, doi: 10.1038/s41598-018-19443-6.

[40] S. Sayed, S. Hong, and S. Datta, "Multi-terminal spin valve on channels with spin-momentum locking," *Sci. Rep.*, vol. 6, Oct. 2016, Art. no. 35658, doi: 10.1038/srep35658.

[41] S. Sayed, S. Hong, and S. Datta. (Dec. 2017). "Transmission line model for charge and spin transport in channels with spin-momentum locking." [Online]. Available: https://arxiv.org/abs/1707.04051

[42] S. Sayed, S. Hong, E. E. Marinero, and S. Datta, "Proposal of a single nano-magnet memory device," *IEEE Electron Device Lett.*, vol. 38, no. 12, pp. 1665–1668, Dec. 2017, doi: 10.1109/LED.2017.2761318.

[43] J.-H. Lee *et al.*, "Multi-terminal spin valve in a strong Rashba channel exhibiting three resistance states," *Sci. Rep.*, vol. 8, no. 1, 2018, Art. no. 3397, doi: 10.1038/s41598-018-21760-9.

[44] D. Vodenicarevic *et al.*, "Low-energy truly random number generation with superparamagnetic tunnel junctions for unconventional computing," *Phys. Rev. Appl.*, vol. 8, no. 5, p. 054045, 2017, doi: 10.1103/PhysRevApplied.8.054045.

[45] K. Y. Camsari, S. Salahuddin, and S. Datta, "Implementing p-bits with embedded MTJ," *IEEE Electron Device Lett.*, vol. 38, no. 12, pp. 1767–1770, Dec. 2017, doi: 10.1109/LED.2017.2768321.

[46] B. Sutton, K. Y. Camsari, B. Behin-Aein, and S. Datta, "Intrinsic optimization using stochastic nanomagnets," *Sci. Rep.*, vol. 7, 2017, Art. no. 44370, doi: 10.1038/srep44370.

[47] B. Behin-Aein, V. Diep, and S. Datta, "A building block for hardware belief networks," *Sci. Rep.*, vol. 6, 2016, Art. no. 29893, doi: 10.1038/srep29893.

[48] K. Y. Camsari, R. Faria, B. M. Sutton, and S. Datta, "Stochastic p-bits for invertible logic," *Phys. Rev. X*, vol. 7, no. 3, p. 031014, 2017, doi: 10.1103/PhysRevX.7.031014.

Authors' photographs and biographies not available at the time of publication.